

UNCLASSIFIED

Defense Technical Information Center
Compilation Part Notice

ADP013592

TITLE: Simulations of Internal-Wave Breaking and Wave-Packet
Propagation in the Thermocline

DISTRIBUTION: Approved for public release, distribution unlimited

This paper is part of the following report:

TITLE: From Stirring to Mixing in a Stratified Ocean. Proceedings
Hawaiian Winter Workshop [12th] Held in the University of Hawaii at
Manoa on January 16-19, 2001

To order the complete compilation report, use: ADA412459

The component part is provided here to allow users access to individually authored sections
of proceedings, annals, symposia, etc. However, the component should be considered within
the context of the overall compilation report and not as a stand-alone technical report.

The following component part numbers comprise the compilation report:
ADP013572 thru ADP013596

UNCLASSIFIED

Simulations of internal-wave breaking and wave-packet propagation in the thermocline

G.F. Carnevale

Scripps Institution of Oceanography, University of California San Diego, 9500 Gilman Drive, La Jolla, California 92093, USA

P. Orlandi

Dipartimento di Meccanica e Aeronautica, University of Rome, "La Sapienza," via Eudossiana 18, 00184 Roma, Italy

M. Briscolini

IBM Italia S.p.A., Via Shangai 53, 00144 Roma, Italy

R.C. Kloosterziel

School of Ocean and Earth Science and Technology, University of Hawaii, Honolulu, 1000 Pope Rd, Hawaii 96822

Abstract. An investigation into density and velocity fluctuations in the oceanic thermocline is presented. Two kinds of numerical simulation are reported. In the first, an attempt is made to capture the transition from breaking internal waves to the small-scale turbulence they generate. The model used for this is based on a continual forcing of a large-scale standing internal-wave. Evidence is presented for a transition in the energy spectra from the anisotropic k^{-3} buoyancy range to the small-scale $k^{-5/3}$ isotropic inertial range. Density structures that form during wave breaking are analyzed and regions of mixing associated with the breaking events are visualized. In the second kind of simulation, internal-wave packets are followed as they propagate through the thermocline. It is found that the breaking of crests within the packet can lead to overturning events on the scale observed in the ocean, and the subsequent turbulence can form a continuous wake.

Introduction

In recent observations of fluctuations in the oceanic thermocline, *Alford and Pinkel* (1999, 2000) found many overturns with vertical scale of about 2 m and these were highly correlated with the presence of energetic waves with vertical wavelengths on the order of 10 m. Large scale fluctuations, say 10 m and above in vertical scale, can be described reasonably well as internal waves. For much smaller scales, say 1 m and below, the flow is probably better described in terms of nearly isotropic turbulence. Intermediate between the large-scale wave dynamics and the small-scale turbulence is a transition regime in which there is a competition between waves and turbulence. It is this intermediate range, often called the buoyancy range, that contains the overturning activity observed by Al-

ford and Pinkel. Since the observations are essentially one-dimensional in space, a direct numerical simulation which could faithfully describe events in this range would help toward understanding the full three-dimensional flow structures behind the observations. The first part of our investigation will focus on the production of overturns by an idealized internal wave forcing.

The second part of our investigation concerns the propagation of internal-wave packets through the thermocline. *Alford and Pinkel* (1999, 2000) observed coherent regions of strong oscillatory vertical strain rate that travel vertically through 100 m or more of the thermocline. These propagating structures had an internal wave structure with vertical wavelength of about 10 m, and the entire coherent region could be described by

an envelope of about 50 m in vertical extent. These coherent structures were strongly correlated with 2 m overturns. Given the complicated nature of the flow, with strong components of large-scale advection, it was difficult to know precisely what kind of structures to associate with these coherent localized oscillations. *Alford and Pinkel* suggested that these were internal-wave packets. Here we hope to validate that identification to a certain extent by showing how an idealized packet would propagate through a simplified model of the thermocline, and by showing that the observed overturning scales could be consistent with internal-wave packet propagation.

Given current computer resources, it would not be practical to simulate all of the scales that are relevant to the breaking of waves in the buoyancy range. The forcing of the waves is thought to result from a complicated interaction of many internal waves with scales ranging in the vertical from 10's of meters to hundreds of meters and more, and typical horizontal internal wave scales can be even much greater than these. On the small-scale end of the spectrum, the observed breaking is occurring on vertical scales of the order of 1 m, and these breaking events produce turbulence that extends down to a viscous cutoff on the order of 1 cm. Thus direct numerical simulation of the entire range of scales is still impractical. We will use a combination of LES modeling and an artificial model of the large scale forcing in order to reduce the spectral range that we will need to cover. To attack our first problem of investigating how waves at the short-scale end of the Garrett-Munk (1975) spectrum go unstable and break in the buoyancy range, we have used an artificial forcing with length-scales fixed at 20 m in the vertical and 20 m in the horizontal to represent the effect of all larger scales. At the small-scale end of the simulation, we have introduced an eddy viscosity with a cutoff at the 16 cm level in both horizontal and vertical directions. Thus our model does some violence to the true physics at the large and small-scale ends of the simulated range. However, the hope is that it will do justice to the evolution in the buoyancy range. This model does prove capable of capturing the transition from the buoyancy to the inertial range. For the problem of wave-packet propagation, which is perhaps the source of the order 10 m scale variability most correlated with overturning, we needed to expand our domain size in order to allow for the propagation and evolution of the packet.

Forced 20-meter wave

Our first goal is to determine to what extent our simulations can capture the transition from the buoyancy range to the inertial range in the energy spec-

tra. Constructing a theory of this transition is complicated because of the anisotropy of the buoyancy range. To make progress, some theoretical formulations have represented the entire spectrum as depending only on wavenumber k . The model for the kinetic energy spectrum in the buoyancy range is then

$$E(k) = \alpha N^2 k^{-3} \quad (1)$$

where α is an empirical constant and N is the Brunt-Väisälä frequency, which measures the strength of the stratification. The Brunt-Väisälä frequency is defined by

$$N^2 = -\frac{g}{\rho_0} \frac{\partial \bar{\rho}}{\partial z} \quad (2)$$

where g is the acceleration of gravity, $\bar{\rho}$ is the background density profile, assumed stable (i.e. $\partial \bar{\rho} / \partial z < 0$), and ρ_0 is the volume average of $\bar{\rho}$. From the observed spectra of vertical shear, the constant α is determined to be about 0.47, but it will be more convenient for us to consider the two components of the horizontal velocity (u, v) separately, and, assuming horizontal isotropy in the observations, this would suggest $\alpha \approx 0.2$ for the spectrum of either component (cf. *Gibson 1986, Gargett et al. 1981*). The inertial range kinetic energy spectrum is given by

$$E(k) = C_K \epsilon^{2/3} k^{-5/3} \quad (3)$$

where ϵ is the turbulent dissipation rate of total kinetic energy and C_K is the empirical Kolmogorov constant. A reasonable value to assume for C_K is 1.5 (cf. *Lesieur, 1997*). For the energy of one component of the velocity field, there would simply be a prefactor of 1/3 multiplying this isotropic spectrum. The Ozmidov (or buoyancy) wavenumber is then estimated by simply matching these two spectra at wavenumber k_b . The result is, up to an order one multiplicative constant,

$$k_b \equiv \sqrt{N^3 / \epsilon}, \quad (4)$$

(cf. *Holloway, 1981; Gibson 1986*).

The model for the potential energy spectrum in the buoyancy range is similar to that for the kinetic energy spectrum. The empirical constant α for the temperature spectrum is found to have value of about 0.2 (cf. *Gibson 1986, Gregg 1977*). The spectral model for the inertial range of density fluctuations is the Corrsin-Obukhov spectrum, which involves the decay rate of density fluctuations as well as ϵ . For our purposes, we prefer to write the spectrum directly in terms of the turbulent decay rate of potential energy, which we shall write as ϵ_{pe} . Then the Corrsin-Obukhov spectrum for the potential energy takes the following form:

$$PE(k) = C_o \epsilon_{pe}^{-1/3} k^{-5/3}, \quad (5)$$

where C_o is the Corrsin constant.

For all of the simulations presented here, we have used the Boussinesq approximation. The evolution equations may be written as

$$\frac{\partial \mathbf{u}}{\partial t} + \mathbf{u} \cdot \nabla \mathbf{u} + \frac{1}{\rho_0} \nabla p' - \frac{\rho'}{\rho_0} \mathbf{g} = \nu(\nabla^2) \nabla^2 \mathbf{u}, \quad (6)$$

$$\nabla \cdot \mathbf{u} = 0. \quad (7)$$

$$\frac{\partial \rho'}{\partial t} + \mathbf{u} \cdot \nabla \rho' + w \frac{\partial \bar{\rho}}{\partial z} = \kappa(\nabla^2) \nabla^2 \rho', \quad (8)$$

where $\nu(\cdot)$ and $\kappa(\cdot)$ are considered functions of the Laplacian operator and are used to represent eddy parameterizations in general (cf. *Herring and Metais* 1992) and $\mathbf{g} = -g\hat{z}$. We have neglected the effect of rotation, which should not play a major role at the small scales with which we are concerned. The total density is given by

$$\rho = \bar{\rho}(z) + \rho'(x, y, z, t), \quad (9)$$

where $\rho'(x, y, z, t)$ is the deviation from the horizontally averaged density $\bar{\rho}(z)$. ρ_0 is the average of $\bar{\rho}(z)$ over z . The pressure p' is the deviation from the background mean pressure. p' can be determined in terms of \mathbf{u} by taking the divergence of (6) under the assumption that the velocity field is divergenceless.

We simulate these dynamical equations with a spectral code with triply periodic boundary conditions. As a sub-grid scale parameterization, we have used the large-eddy simulation model of *Lesieur and Rogallo* (1989). This eddy viscosity $\nu_t(k)$ is approximately constant throughout the buoyancy range and the large-scale end of the inertial range, but increases rapidly with k in the vicinity of the spectral cutoff k_c . Due to the spectral shape of the eddy viscosity, this model is sometimes called the cusp model. It seems reasonable in modeling the buoyancy range to use such a model since it does not completely neglect the effects of unresolved eddies on the buoyancy range, but, at the same time, it puts the strongest eddy viscosity in the inertial range near the cutoff.

We should emphasize the point that the size of the eddy viscosity depends on the amount of energy at the cutoff scale. If the resolution of the simulation of a given physical flow is increased, that is if k_c is increased, then the eddy viscosity will be correspondingly smaller. The total viscosity used in the simulations is the sum of the eddy viscosity and the constant molecular viscosity ν_{mol} . Thus the $\nu(\nabla^2)$ in equation (6) in the spectral simulation is taken as the total viscosity:

$$\nu(k) = \nu_{mol} + \nu_t(k) \quad (10)$$

The choice of turbulent diffusion depends on the choice of values for various parameters that enter into

the closure model for stratified turbulence. For simplicity, we have just taken the turbulent Prandtl number $Pr_t(k)$ to be a fixed constant independent of k in our simulations. We determined this constant by examining the evolution of the potential energy spectrum for decaying stratified turbulence that is initially highly excited at all scales. More specifically, we started with an initial spectrum in which the GM spectrum was continued to scales below 10 m as in the decay simulations of *Siegel and Domaradzki* (1994). With $Pr_t = 0.55$ our simulations of decaying turbulence produced spectra with the high wavenumbers obeying the $k^{-5/3}$ law for both velocity and density fluctuations.

Next we turn to the question of the forcing. The large-scale flows that actually drive the buoyancy range are predominantly the waves of the Garrett-Munk range. The full range where internal wave dynamics dominates includes scales of kilometers in the horizontal and hundreds of meters in the vertical. Because of lack of resolution, we cannot provide a full representation of the effects of all large-scale internal wave forcing on the buoyancy range. In our model, of necessity, we perform a drastic reduction in modeling the forcing; we replace the driving of all of the GM waves by a linear standing wave at one wavelength. *Bouruet-Aubertot et al.* (1995, 1996), in two-dimensional simulations of a stratified turbulence, excited a standing wave of the type we use, but they allowed this wave to decay, whereas we maintain its amplitude at the same level throughout the simulation.

To give the form of the forcing used, let us first introduce nondimensional units. We will take all lengths to be scaled by $2\pi/L$, where L is the length of one side of our computational domain. Time will be scaled by $1/N$. Then the frequency of linear internal waves is given by

$$\sigma = \pm \frac{k_h}{k}, \quad (11)$$

where $k_h = \sqrt{k_x^2 + k_y^2}$ is the horizontal wavenumber. One particular linear standing wave is

$$\mathbf{u} = (u, v, w) = A \frac{g^*}{\sqrt{2}} (0, \sin y \sin z, \cos y \cos z) \sin \frac{t}{\sqrt{2}}, \quad (12)$$

$$\frac{\rho'}{\rho_0} = A \cos y \cos z \cos \frac{t}{\sqrt{2}}, \quad (13)$$

where A is an arbitrary amplitude and g^* is the nondimensional gravity. Note that the dimensional period of this wave, which is the forcing period, is given by

$$T_F = \sqrt{2} \frac{2\pi}{N}. \quad (14)$$

To give some idea of the structure of this standing wave, we show in Figure 1 a contour plot of the density

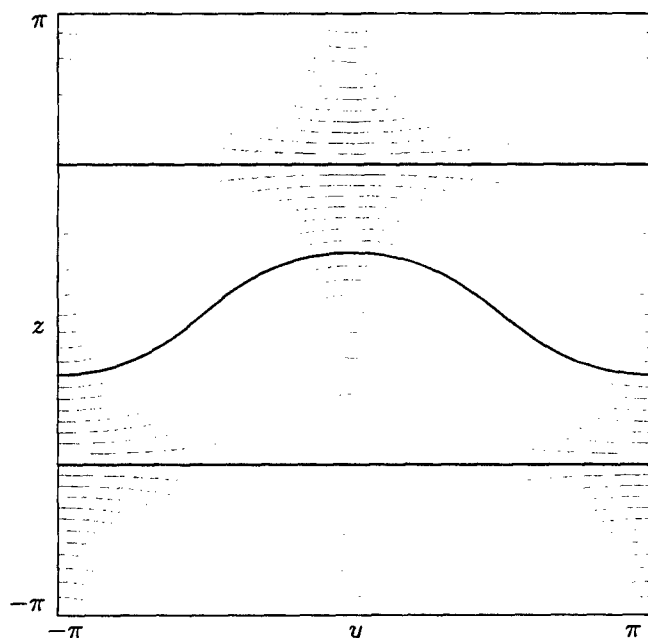


Figure 1. Contour plot of the density field in a vertical y - z cross section through the center of the domain. The width and height of the cross section are each 20 m, which corresponds to 2π in nondimensional units. The instant shown corresponds to maximum displacement of the isopycnals for the forced standing wave.

field in a vertical y - z cross section. Note that the density field in this standing wave has no variation along the x direction. In this figure, we see an instantaneous representation of the iso-density surfaces. When $t/\sqrt{2}$ is an odd multiple of $\pi/2$, these isopycnals will all be flat. The degree to which they deviate from that at other times depends on the value of A as well as t . The instant of time represented here is such that $t/\sqrt{2}$ is an integer multiple of π and, hence, one of maximum distortion of the density contours. Note that the density field in (13) has two nodal planes, represented by two thick contour lines in the figure, at $z = \pm\pi/2$ (nondimensional). During the forcing cycle, these planes remain flat and fixed in position. The fluid above and below these planes vertically approaches and retreats from them depending on the phase in time and the y position considered. Thus the points on the nodal planes at $y = 0$ and $y = \pm\pi$ are the centers of regions of oscillating high strain rate. On the other hand the points where the isopycnals are steepest, that is where $y = \pm\pi/2, \pm3\pi/2$ and $z = 0, \pm\pi$ the magnitude of the shear $\partial v/\partial z$ is highest. Thus one advantage of the standing wave forcing is that the points of highest shear and highest strain rate remain fixed in space making it easier to differentiate the kinds of overturning events associated with these extremes. This will be convenient for making comparisons with *Alford and*

Pinkel's (2000) analysis. In particular, they noted that there were regions of high shear where classical shear instabilities often, but not always, resulted in overturning. Even more more interestingly, there were regions of high Ri in which overturns were also observed. In more than half of these cases Ri was even greater than 2 suggesting that the typical shear instability ($Ri < 1/4$) is unlikely. Many of these overturns were in regions of high vertical strain rate. With our standing wave forcing, the regions of high shear and high strain rate are separate and each occur in the same location during each forcing oscillation. This helps simplify the analysis.

In two-dimensional numerical studies of *Bouruet-Aubertot et al.* (1996), the standing wave becomes unstable and generates turbulence. This would also happen in our three-dimensional simulation, but the turbulence would be highly constrained since there is yet no source of x -variation in our flow. To break the two-dimensional symmetry of the flow, while maintaining the basic structure of the large scale, we add a weak component of forcing with x -variation. We have tried this in various ways: adding a random initial perturbation at all scales, randomly forcing the modes with $k = 1$ at each time step, adding another large-scale standing wave, adding a propagating wave, and so on. The results are similar to each other if the perturbations are sufficiently weak. For the simulations discussed below, we have added to the primary forcing wave only a small amplitude standing wave of the same spatial scale. Specifically, we added the following perturbation:

$$\mathbf{u} = A' \frac{g^*}{\sqrt{2}} (\cos(x+z), 0, -\cos(x+z)) \sin \frac{t}{\sqrt{2}}, \quad (15)$$

$$\frac{\rho'}{\rho_0} = A' \cos(x+z) \cos \frac{t}{\sqrt{2}}. \quad (16)$$

Thus in the simulations discussed below the forcing occurs only at $k = \sqrt{2}$. The coefficient A' was taken to be $A/20$, and, hence, the energy in the perturbation is only $1/400$ that of the primary forcing wave.

We performed a series of experiments in which the size of the computational domain and the amplitude of the forcing were varied. The initial studies were at resolution 64^3 and showed that for sufficiently large amplitudes A for which the forcing wave itself was overturning, a $k^{-5/3}$ spectrum extending over most of the spectral range could be established. For weaker forcing, a steeper spectrum approximating k^{-3} was found (*Carnevale and Briscolini*, 1999). For intermediate amplitude forcings, we were able to observe, at least intermittently, cases which do appear to exhibit the transition from the buoyancy range to the smaller scale inertial range. Weak and strong forcings are measured relative to shear amplitudes typical in the thermocline.

The best results were obtained with a forcing amplitude that could actually be considered representative of wave amplitudes in the thermocline. Specifically, the forcing amplitude that we refer to as intermediate, is for a value of A in equations (12) and (13) such that the maximum shear during a cycle of the forcing is equivalent to the rms shear of the GM spectrum at the scale of our computational domain. The rms shear is calculated by integrating the shear of the GM spectrum from the kilometer scale down to the scale of interest (cf., Gregg, 1989). Our best results tended to be for cases in which the vertical wavelength of the forcing was 20 m. For $N = 3$ cph, the net rms shear from the GM spectrum for this scale is $S_{GM}(20\text{ m}) \approx 3 \times 10^{-3} \text{ s}^{-1}$ (cf., Gregg, 1989). Taking this value to determine the amplitude of our forcing, we obtain a standing wave in which the largest deviation of the density isosurfaces are as illustrated in Figure 1. Thus we have a standing wave that does not itself overturn during the forcing cycle, and, in addition, the Richardson number of the forcing wave, defined by

$$Ri \equiv -\frac{\frac{g}{\rho_0} \frac{\partial \rho}{\partial z}}{\left(\frac{\partial u}{\partial z}\right)^2 + \left(\frac{\partial v}{\partial z}\right)^2}, \quad (17)$$

does not drop below 3.125. Therefore, the forcing wave itself is convectively stable and not subject to shear instability. This kind of forcing is consistent with the picture that the GM waves themselves are not convectively or shear unstable, but through wave-wave interactions will produce smaller scale waves that are unstable by these criteria. Choosing a stronger forcing wave that is itself convectively or shear unstable would miss the important cascade process that produces the unstable waves of the buoyancy range, but would rather produce turbulence directly resulting in an inertial range (cf. Carnevale and Briscolini, 1999).

For all of the simulations discussed below, we used a resolution 128^3 and a computational cube of 20 m on a side. Our isotropic spectral cutoff is at wavenumber 60, and the smallest resolved wavelength is about 33 cm (with grid spacing $20\text{ m}/128 \approx 16\text{ cm}$). The forcing amplitude was fixed so that the max shear in the forced wave is $S_{GM}(20\text{ m})$, and the Väisälä frequency was taken to be 3 cycles per hour, which is a typical oceanic value.

A long simulation was performed with realistic values for the molecular viscosity and diffusivity. The kinematic viscosity was set to $\nu_{mol} = 0.01\text{ cm}^2/\text{s}$ and the molecular Prandtl number at $Pr_{mol} = 7$ (cf. Gargett, 1985). We can calculate a Reynolds number for the oceanic flow for vertical motions on the 20 m scale by using the rms shear. Thus we can write

$$Re = S_{GM}(L)L^2/\nu_{mol}. \quad (18)$$

For $L = 20\text{ m}$, this Reynolds number would be approximately 10^5 . By including the molecular viscosity, the simulation is an attempt to represent flow with this Reynolds number. We will see that there is not much difference with results obtained by neglecting the molecular components of viscosity and diffusivity. That is to say that over the range of scales simulated (20 m to 33 cm) the difference between infinite Reynolds number flow and that for $Re = 10^5$ is small.

We can think of our standing wave forcing as the linear superposition of a set of propagating internal waves. To be precise, the combination of the two standing waves given in (12) and (15) consists of 12 propagating plane waves. These wave interact nonlinearly producing smaller-scales that eventually fill out the entire spectrum. The early evolution is essentially just that of the nearly two-dimensional standing wave. During this time there are only sinusoidal waves on the most disturbed isosurface, but these waves then fold over forming elongated overturns. These regions are convectively unstable and break. At this point the three dimensionality of the flow becomes evident.

After about five cycles of the forcing, the large-scale wave breaks repeatedly, however, not necessarily during each forcing period. The wave breaking on the most disturbed isopycnal occurs roughly symmetrically with large-scale overturning occurring nearly at the same values of y and z each time and along lines of constant x , respecting in the large scales the symmetry of the main part of the forcing. However, no two breaking events with the subsequent evolution during the forcing cycle are the same. In Figure 2, for one such cycle, we show eight instantaneous images of this isosurface using a perspective three-dimensional plot. The frames are ordered temporally from left to right and top to bottom. The first frame in the upper left hand corner corresponds to $t = 11.39T_F$, and the interval between frames is $\Delta t = T_F/7$. Thus the first and last frames correspond to the same phase of the forcing. The first frame captures the moment when breaking is just beginning. Let us say that the first four frames represent the breaking event, and the last four the aftermath. We see that during the breaking event, heavy fluid spills over lighter fluid, crashing down with the creation of small-scale structures all along the lines of the two breaking regions. Similar behavior is in laboratory experiments with standing-wave forcing (Taylor 1992, McEwan 1983a). Afterwards, the region of the small-scale turbulent structures spreads, eventually 'contaminating' the entire isosurface. If we compare the final frame with the first frame, we see that the final surface is much rougher, filled with small-scale structures everywhere, and that there is no larger scale folding-over of the surface as there was in the first frame. In the

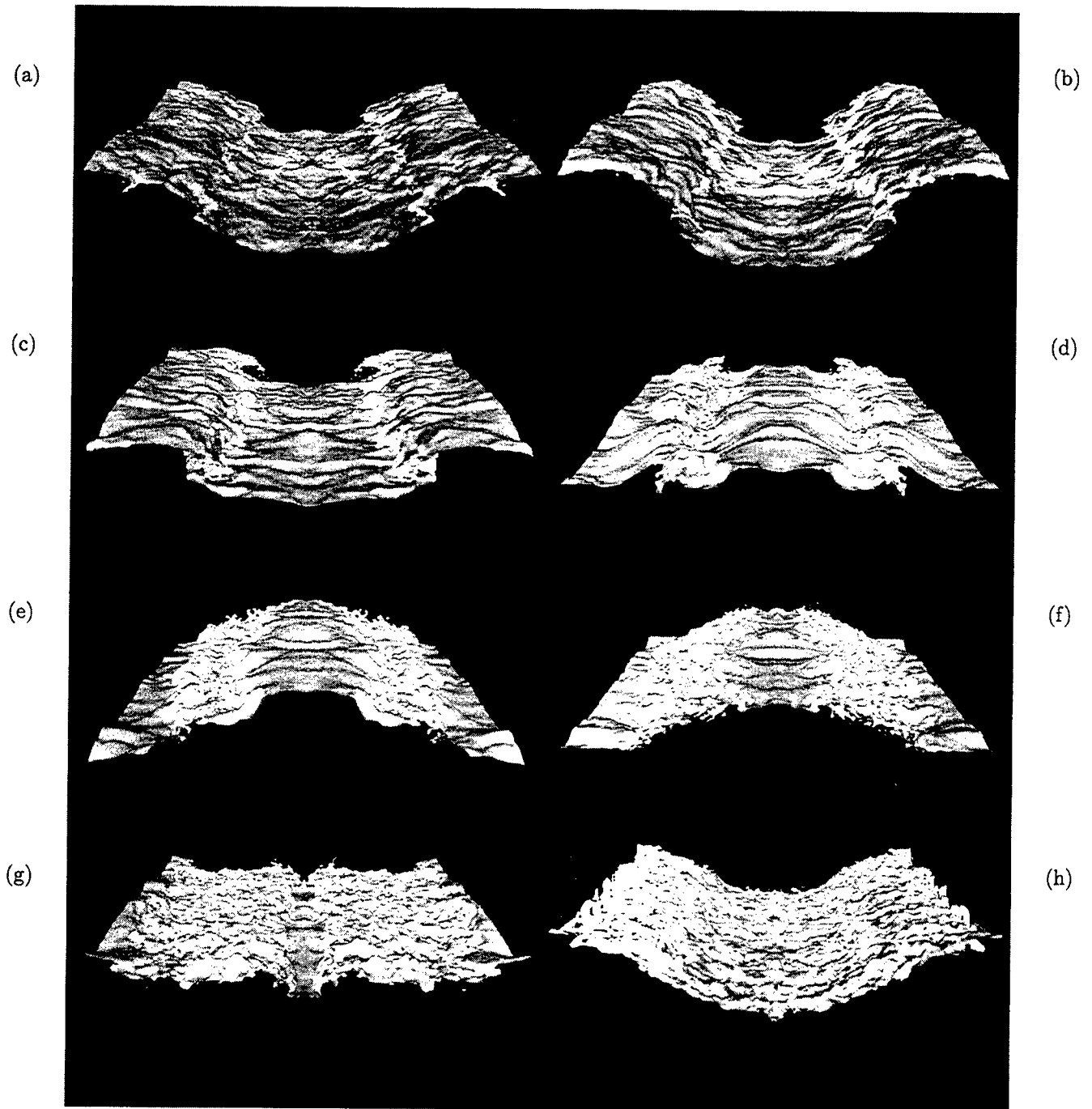


Figure 2. The evolution of the $\rho = \rho_0$ isopycnal during one cycle of the forcing. The frames are ordered by time from left to right and top to bottom. The first corresponds to $t = 11.39T_F$, and the interval between frames is $\Delta t = T_F/7$.

later evolution, the wave will break again, but only after a refractory period, in this case of about two forcing cycles.

Next we will consider the energy spectra for the flow at the same times as those illustrated in Figure 2. Since the energy is highly anisotropic at scales larger than those in the inertial range, plotting the total energy as a function of the isotropic wavenumber tends to obscure the transition between small and large scales. To most clearly display the transition, we have found it useful to consider the spectrum $E_v(k)$ of v , the y component of velocity, which is the horizontal component that is directly affected by the forcing. Along with the spectra, we have also drawn lines corresponding to the inertial range spectrum $(1/3)C_K\epsilon^{2/3}k^{-5/3}$ and buoyancy range spectrum $0.2N^2k^{-3}$. For each frame, ϵ is taken as the total kinetic energy dissipation rate at that time. We have included a factor of $(1/3)$ which is appropriate for a single component in the isotropic inertial range. For the Kolmogorov constant, a value of 1.5 was used in each case. We should emphasize that no attempt is made here to fit the data, but the coefficient is just taken as this standard value *a priori*. For the buoyancy range spectrum, we have used the coefficient $\alpha = 0.2$ in all cases. In each frame shown in Figure 3, we see a fairly good match at wavenumbers greater than about 20 (that is for scales below about 1 m) to the Kolmogorov inertial range spectrum. The main deviation is at wavenumbers near $k = 60$, the cutoff wavenumber, and this is to be expected from previous experience with the cusp model (cf. *Lesieur and Rogallo, 1989*). The spectrum below wavenumber 20 is naturally far more irregular than that above due to the much smaller number of modes in the lower spectral bands. If we neglect the first few wavenumbers, then there is some evidence here for a steeper spectral range for wavenumbers below about $k = 20$, that is for scales larger than about 1 m, at least in the frames that correspond to times during the breaking of the wave (first four panels). In the aftermath of breaking, the spectra tend to be somewhat flatter (the last four panels). The best representative of the transition between buoyancy and inertial range is found in panel (c), which corresponds to a time when the enstrophy is near a local maximum. Here the buoyancy range spectrum makes a reasonably good fit in the range of scales from about 4 m down to about 1 m. From the forcing scale (20 m vertical) to about the 5 m scale, there is a dip in the energy that has also been seen in the spectra from similar two-dimensional simulations of the decay of a standing wave (*Bouruet-Aubertot et al. 1996*).

In this experiment it appears that the expected spectral signature of a transition between a buoyancy range at large scale and the inertial range at small scale oc-

curs only for periods during which there is active breaking. Indeed, it appears that wave-wave interactions repeatedly build up energy in the buoyancy range until a k^{-3} spectrum is achieved. At that point significant breaking occurs and energy drains from the buoyancy range. Let us focus on the breaking event. In Figure 4a is the image of the $\rho = \rho_0$ isosurface at the time identified as the best for illustrating the spectral transition from the buoyancy to the inertial range. It shows the curling over and spilling down or plunging of the heavier fluid over lighter, while Figure 4b suggests mixing by the appearance of many small-scale structures along the two parallel lines of the breaking wave. The corresponding spectra for all three components of kinetic and for the potential energy are shown in Figure 5. First we notice that although the spectra are highly anisotropic from the forcing scale (20 m) down to about the 1 m scale, there is an approximate 'return' to isotropy for the smaller scales. This is particularly evident in the kinetic energy spectra for $t = 11.82 T_F$ (panel c). In panels (a) and (c), we have made an attempt to draw the best fit inertial range spectra to determine the appropriate Kolmogorov constants (C_K) that fit these data. We did this for the $E_v(k)$ spectra, obtaining the best fit 'by eye' from enlarged portions of the small scale spectra. The result that was used to draw the inertial range model spectra in panels (a) and (c) is $(C_K) = 1.4$. In panels (b) and (d), the potential energy spectra are drawn. In these panels the small scales were fit to the Corrsin-Obukhov spectrum to determine the appropriate Corrsin constant. In panels (b) and (d) the Corrsin constants used to draw the model Corrsin-Obukhov spectrum were $C_o = 0.83$ and 0.8 respectively. In all panels the model buoyancy range spectrum drawn is $0.2N^2k^{-3}$. Thus the Kolmogorov constant found here is somewhat smaller than the empirical values of 1.5 and the Corrsin constant is somewhat larger than the empirical value of 0.67. Nevertheless, the values are remarkably close to the empirical values, given that the spectral width of the inertial range here only covers wavelengths from about 1 meter to about 33 cm. Also the near collapse of the three kinetic energy spectra for small scales is encouraging. Thus it seems that the subgrid scale model is working well at small scales and that the dynamics of the transition from anisotropic buoyancy to the isotropic inertial range is acting as imagined in theoretical models. Finally, we should note that the value of ϵ from the simulations is about one third of the value observed by *Alford and Pinkel (2000)* associated with values of $N = 3$ cph. This appears quite reasonable given the level of modeling we have had to employ for the forcing and subgrid scale vortices.

Besides the kinetic and potential energy spectra, we

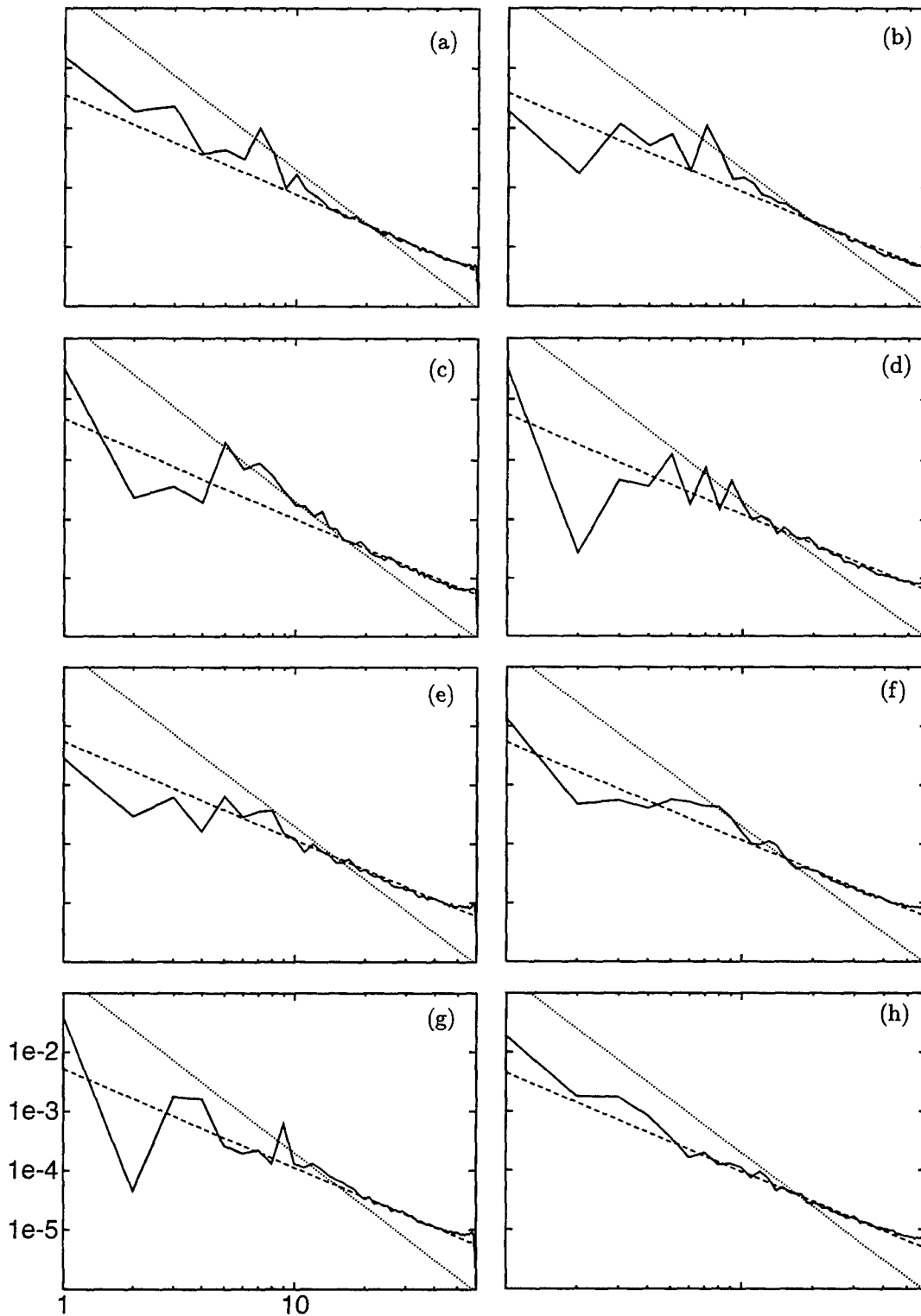


Figure 3. Kinetic energy spectra for the v component of the velocity during one cycle of the forcing. The dashed lines correspond to the Kolmogorov spectrum $(1/3)C_K\epsilon^{2/3}k^{-5/3}$ with $C_K = 1.5$ and the saturation spectrum $0.2N^2k^{-3}$. The time interval between frames is $\Delta T_F/7$ and the first frame corresponds to time $t = 11.39T_F$. These are log-log plots of $E(k)$ in units of $N^2(L/2\pi)^3$ vs. k in units of $2\pi/L$. All plots have the scales as indicated in panel (g).

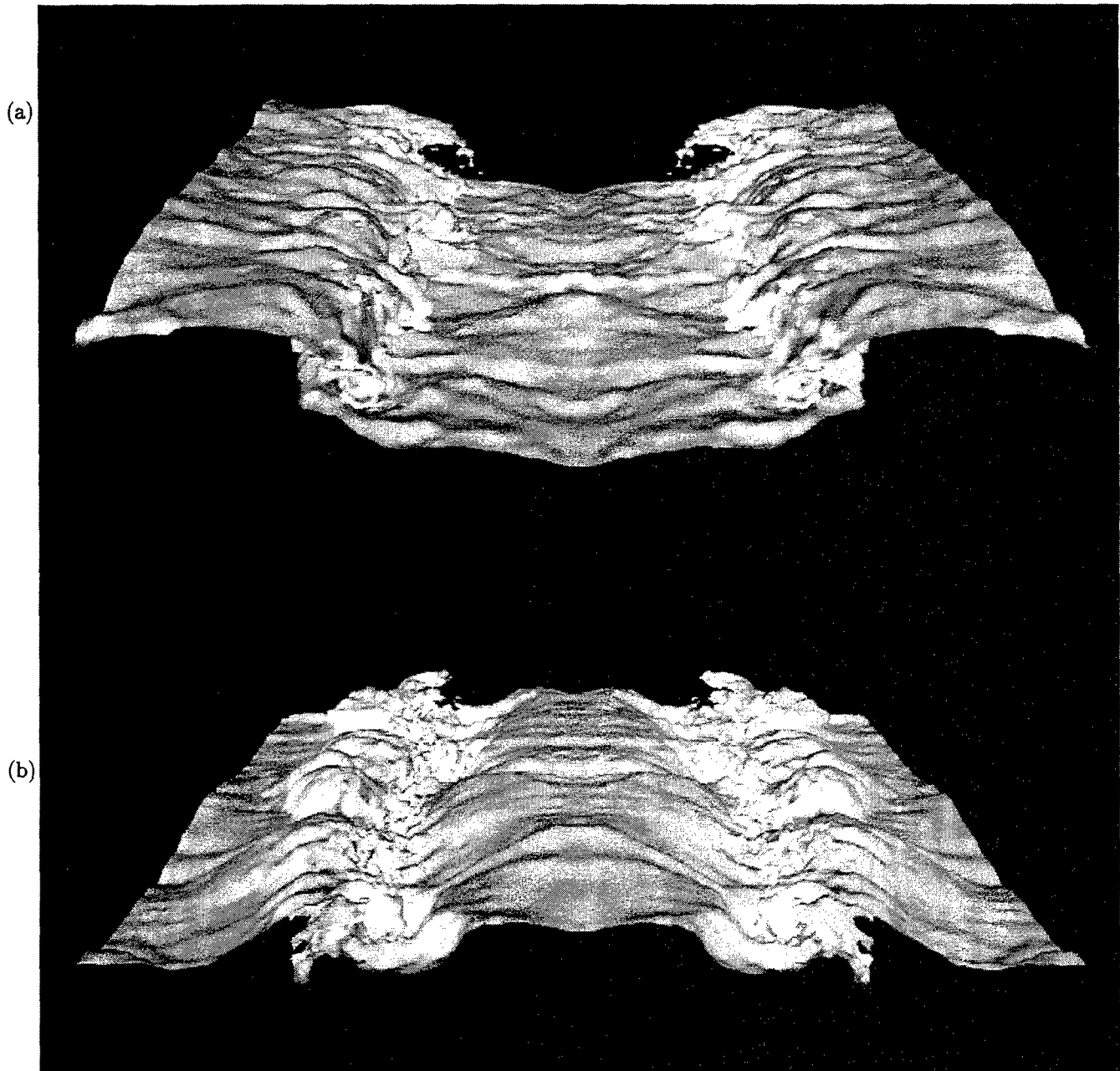


Figure 4. A breaking event visualized on the $\rho = \rho_0$ isopycnal. These are enlargements of the images shown in the composite Figure 2 in panels 3 and 4, corresponding to times (a) 11.68 and (b) $11.82 T_F$ (one seventh of a forcing period apart).

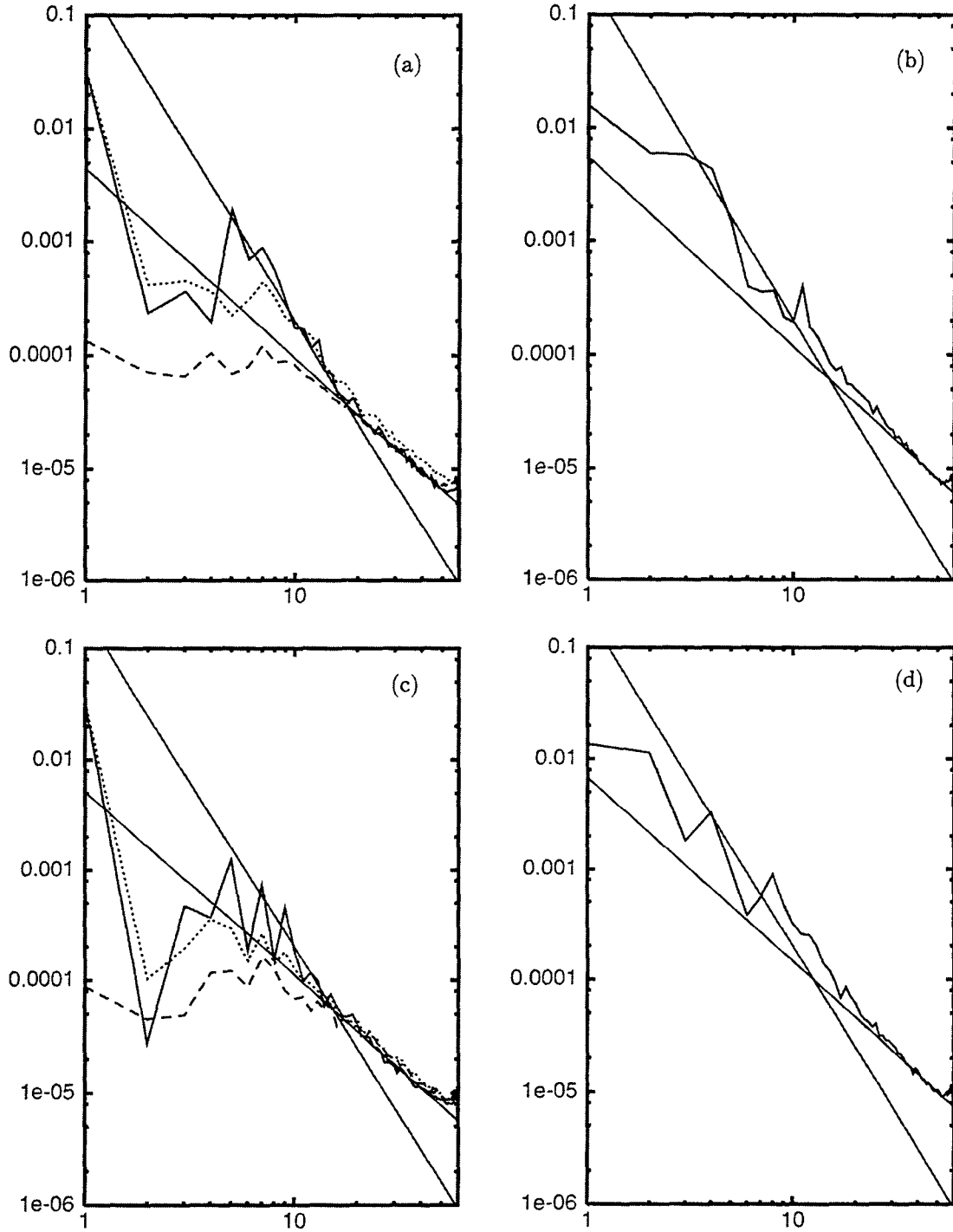


Figure 5. (a) Kinetic energy spectra for all three components of the velocity at time $t = 11.68 T_F$. The thick long dashed, solid and short dashed lines correspond to the energy spectra for the u, v, and w components respectively. The thin solid lines correspond to the Kolmogorov spectrum $(1/3)C_K \epsilon^{2/3} k^{-5/3}$ with $C_K = 1.4$ and the saturation spectrum $0.2 N^2 k^{-3}$. (b) Potential energy spectrum at time $t = 11.68 T_F$. The thick solid line corresponds to the potential energy spectrum. The thin solid lines correspond to the Corrsin-Obukhov spectrum $C_o \epsilon_{pe} \epsilon^{-1/3} k^{-5/3}$ with $C_o = 0.83$ and the saturation spectrum $0.2 N^2 k^{-3}$. (c) As in (a) but for $t = 11.82 T_F$ and $C_K = 1.4$. (d) As in (b) but for $t = 11.82 T_F$ and $C_o = 0.80$.

can also find predictions for the buoyancy flux spectrum in both the theory of Lumley-Shur (cf. Lumley 1964, 1967, Phillips 1967, Weinstock 1985) and the theory of Holloway (1983, 1986). The modal spectrum of the buoyancy flux can be written as

$$-g\mathcal{R} < w_k^* \rho'_k > / \rho_0. \quad (19)$$

If this quantity is positive, then for wavevector k there is conversion of potential energy to kinetic energy, and vice versa if it is negative.

The prediction of the Lumley-Shur theory for the buoyancy flux spectrum in the buoyancy and inertial ranges is

$$BF(k) = -2D \frac{\epsilon_0}{k_b} \left(1 + D(k_b/k)^{4/3}\right)^{1/2} (k_b/k)^{7/3} \quad (20)$$

where k_b is as defined in (4) and D is a constant. Lumley (1964) assumed the buoyancy flux to be negative and, hence, D to be positive. In displaying his final result, Lumley incorporated D into his definition for k_b , but we will leave it explicit. Lumley's prediction of negative buoyancy flux through the buoyancy and inertial ranges is just the opposite of what we have found numerically for our wave-forced problem. All of the ingredients for an alternative prediction of the buoyancy flux are given in Holloway (1983), and based on this we have derived the same prediction as given in (20), but with the sign of D clearly arbitrary (for details see Carnevale et al., 2001).

In Figure 6a, we plot the buoyancy flux spectrum from our simulation as a function of k . This is a time averaged spectrum, where we have averaged over a period of $6T_F$, with time increment of $0.1T_F$. The time averaging is necessary to remove temporal fluctuations in the large-scales. Note that the buoyancy flux spectrum is negative for large scales ($1 < k < 3$), and positive for smaller scales. This implies a transformation of kinetic to potential energy at large scales (closest to the forcing scale $k = \sqrt{2}$) and a transfer of potential to kinetic energy at all smaller scales. Since our observed buoyancy flux spectrum is positive through both the buoyancy and inertial ranges, it can be compared to the theoretical prediction given by (20) only by choosing a negative value for D . To define the constant D , we note that the wavenumber where the buoyancy flux vanishes is determined by D . Here we shall choose D so that the zero value occurs at $k = 3.5$ (corresponding in our simulation to a wavelength of 5.7 m) since our buoyancy flux was found to vanish between $k = 3$ and $k = 4$. The theory will apply only above this wavenumber, and we can think of this as the lower limit on the buoyancy range, or the upper wavenumber of the Garrett Munk spectrum in the schematic shown in our introduction. To compute k_b , given by (4), we use the

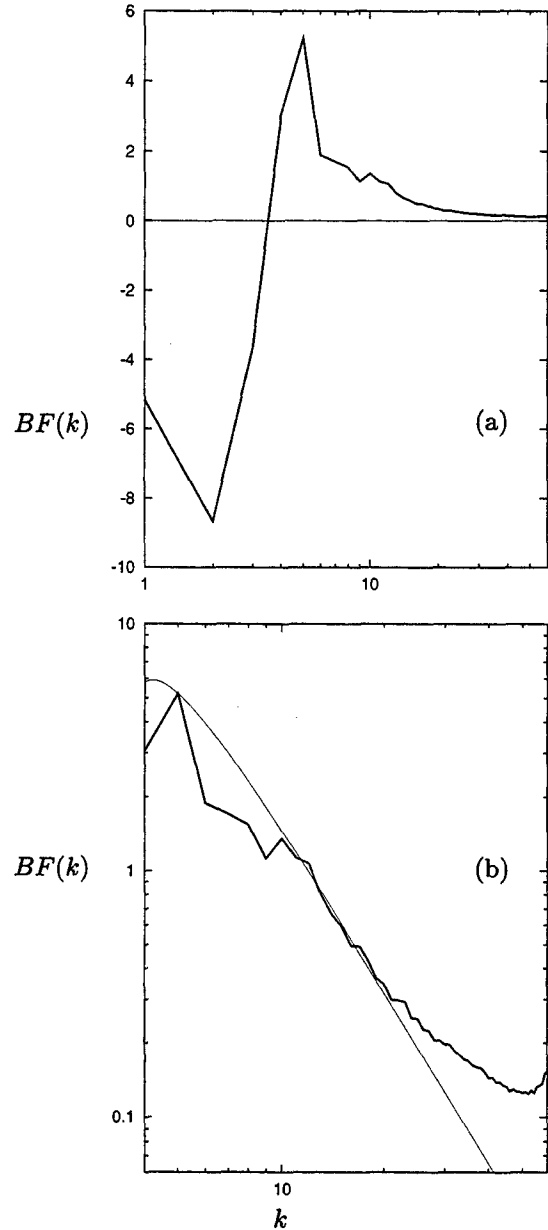


Figure 6. (a) Graph of the buoyancy flux spectrum averaged over 6 periods of the forcing, with 10 samples per period. (b) as in (a) but only the positive portion of the spectrum plotted in log-log format to compare with the theoretical spectrum of equation (20) with negative coefficient D . The result from the simulation is represented by the thick line, while the theoretical spectrum, based on $\epsilon_0 = \bar{\epsilon}$ where the overbar represents time averaging, is drawn as a thin line. All graphs in (a) and (b) are normalized by $\bar{\epsilon}/\kappa_b$.

time averaged dissipation rate $\bar{\epsilon}$. Thus all parameters in the theory are determined by the wavenumber where the buoyancy flux vanishes and the values of N and $\bar{\epsilon}$ (in this case $k_b \equiv (N^3/\bar{\epsilon})^{1/2} \approx 34.1$). The resulting theoretical buoyancy flux spectrum is compared in Figure 6b to the results from our simulation. For wavenumbers in the buoyancy range, the match between theory and simulations is reasonably good. For the theoretical curve, the decay with k is approximately $k^{-7/3}$ for all k above about 10. The simulation data follow the theoretical curve fairly well up to about wavenumber 20, where the simulation spectrum begins to deviate from $k^{-7/3}$, and is clearly much shallower than this for $k \geq 30$. This shallowness of the simulation spectrum for k greater than about 30 is probably an indication that the buoyancy flux is not captured properly by the SGS model near the high wavenumber cutoff. The cusp model viscosity grows rapidly with k for wavenumbers above about $k = 30$ and is largest at k_{max} . This is just the range where our buoyancy flux spectrum becomes very shallow. It is very possible that the artificial damping of the high k modes that the model performs to mimic transfer of energy beyond k_{max} does not allow for the proper treatment of the buoyancy flux in that region. But this is not unexpected for such a subgrid-scale model.

Positive buoyancy flux for small scales has also been found in other simulations. In direct numerical simulations (i.e. simulations without subgrid scale modeling) of forced stratified turbulence in both two and three-dimensions, *Holloway* (1988), and *Ramsden and Holloway* (1992) showed that the buoyancy flux was negative only at large scales and positive at small scales. These results were interpreted as meaning negative buoyancy flux for $k < k_b$ (i.e. in the buoyancy range) and positive buoyancy flux for higher k . However, the forcing used in their simulations was spectrally fairly broad, and it would not be inconsistent with their results to say that the buoyancy flux was negative at the strongly forced modes and positive for smaller scales as in our findings. Additionally, we have repeated our numerical simulations with a finite difference code using a Smagorinsky eddy viscosity, a very independent test, and also found positive buoyancy flux through the buoyancy and inertial ranges. In their finite difference LES study of shear driven stratified turbulence, *Kaltenbach et al.* (1994) also found positive buoyancy flux at small scales and negative at large scales, although we must note that the region of negative buoyancy flux in their simulations is spectrally very broad compared to ours. In two-dimensional flow simulations of the decay of a standing wave of just the type that we use for forcing our flow, *Bouruet-Aubertot et al.* (1996) found that the buoyancy flux was positive through most of the range

that they identified with the buoyancy range, and also that the flux followed a $k^{-7/3}$ spectral law in a run with grid resolution 256^2 and a slightly steeper law at resolution 512^2 (note that those simulations did not include an inertial range).

There was some discussion at the 'Aha Huli'ko'a meeting about the possibility that the sign of the buoyancy flux found in these simulations is affected by the type of forcing used. Our forcing inputs both potential and kinetic energy, while it may be more suitable to consider a source of kinetic energy alone in these problems. If there were no explicit external forcing of the density evolution, then the net buoyancy flux (averaged over time) would have to be negative to balance the drain of potential energy due to diffusion. This however does not mean that the buoyancy flux would have to be negative for all scales. Further simulations would be helpful to define how the buoyancy flux spectrum varies as the mix of kinetic and potential energy sources are changes.

Structures in regions of high strain rate

The main structure of interest in the buoyancy range evident in the density isosurfaces presented in the last section is the overturn produced by the curling over of the isosurface in a manner familiar from surface wave breaking. The overturning region shown in the breaking wave illustrated in Figure 2c has a vertical scale of about 2 meters. This is similar in size to overturns found in oceanographic measurements in the buoyancy range. *Alford and Pinkel* (2000) made an inventory of more than 2200 overturns. They found a median Thorpe scale, a measure of the vertical extent of the overturn, of 1.88 m. Note that this is not greatly different from the scale suggested by the transition point in the spectra shown in Figure 5, where the associated length scale is about 1.2 m. Since the observational data are primarily one-dimensional in space, it is difficult to form a three-dimensional image of those overturns. The ability to perform three-dimensional analysis of such structures is one of the benefits of numerical simulation.

Examining the full density field more thoroughly, we also find interesting structures of a rather different nature than those associated with strong vertical shear. These can be represented well by the deformations of the density surfaces that are the flat nodal surfaces of the forcing wave. We shall just refer to these surfaces as the nodal surfaces even when perturbed and deformed by eddies. The most basic motion of the fluid in the nodal surfaces is alternately toward and away from the centers of high strain; however, the combination of the large-scale background straining motion and small-scale eddies produces localized deformations of the nodal surface that can result in overturning and mixing in a man-

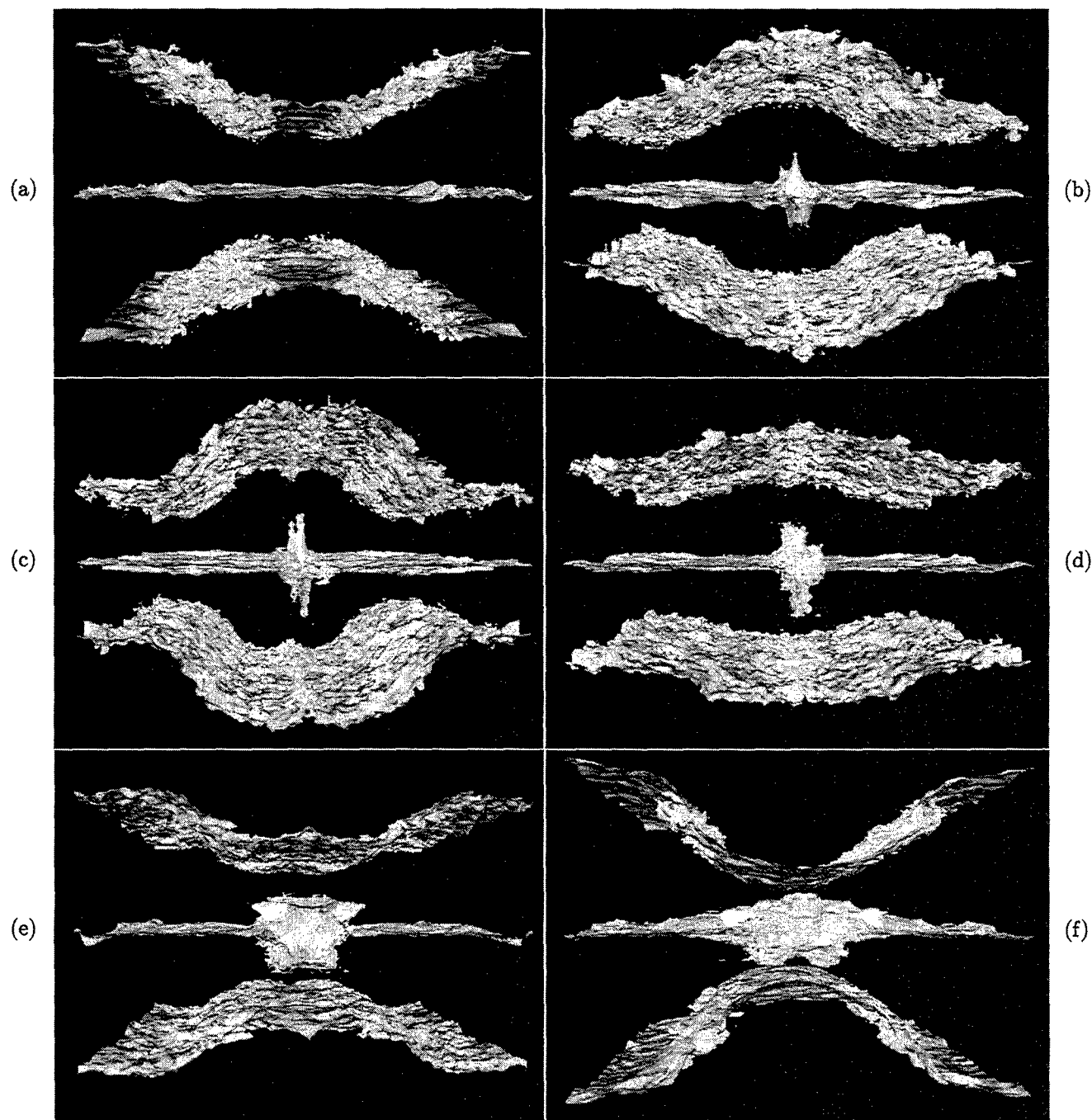


Figure 7. The evolution of three density isosurfaces ($g^*(\rho - \rho_0)/\rho_0 = 0, \pi/2, \pi$) showing the evolution of 'spouts' from a 'nodal surface' and their subsequent collapse with considerable broadening and mixing. Times represented are $t = 12.1, 12.4, 12.5, 12.7, 12.8$, and $13.1 T_F$.

ner different from the overturns discussed in the last section. By plotting simultaneously three density isosurfaces (one 'nodal surface' and the most strongly perturbed isosurfaces above and below it) for a sequence of times during the forcing cycle, we can get some understanding of the nature, formation, evolution, and fate of these structures. In Figure 7, the sequence proceeds from left to right, top to bottom. We have shifted our view of the computational domain by an amount in the vertical sufficient to center the upper 'nodal surface' in the image. Above and below the 'nodal surface,' the most strongly displaced isosurfaces are shown. The upper and lower isosurfaces move vertically but always in opposite directions at any horizontal location. The combined effect of the motion of these surfaces above and below the 'nodal surface' produces vertical 'dilation' and 'compression' centered on the 'nodal surface' without producing large-scale sinusoidal displacement of that surface. In panels (a), (b) and (c), the upper/lower surface is moving upward/downward in the middle of the domain (i.e. at $y = 0$, where y is the horizontal coordinate), and oppositely at the left and right ends of the domain. This is associated with the vertical straining of the nodal surface in the middle and at the left and right ends of the domain. In panel (b) the isosurface 'erupts' with elements moving up and down along a midline pointing into the plane. The eruption reaches its maximum extension when the upper and lower surfaces stop their motion, and reverses direction around the time of panel (c). At $y = 0$ on the 'nodal surface' this is a time of maximum vertical dilational strain but zero strain rate (where $\partial w / \partial z$ is the vertical strain rate). The structures formed by these eruptions represent localized intrusions of heavy fluid into light fluid and vice versa. We shall refer to them as 'spouts.' As the upper and lower isosurfaces move back toward the 'nodal surface,' the sense of straining motion is reversed and the spouts that were formed are flattened. This causes a spreading out of these structures, which in some cases results in tossing elements of the spouts to the right and left of the midline. This leads to the kind of pattern seen in panel (e) which is in part an elongated horizontal structure as opposed to the elongated vertical structures originally produced during the vertically dilational phase of the large-scale straining motion. The final panel (f) shows the isosurface a short time after the upper and lower surfaces have again reversed their direction of vertical motion. This is a phase of the motion near to that of the initial panel (a), but now there is a mixed patch of fluid at the mid section ($y=0$) of the 'nodal surface.'

To summarize, we can say that the 'spouts' originate from small-scale deviations of the nodal surface created by turbulent flow at the nodal surface. Once

perturbations pull structures from the nodal planes vertically, these elements are subject to advection due to the large-scale straining motion of the forcing wave. At times and positions where the straining is highly dilational in the vertical, these deviations from the flat plane elongate vertically and narrow horizontally, forming 'spouts.' Then, during the vertically compressional and horizontally dilational phase of the forcing, the spout is elongated horizontally creating regions of convectively unstable overturned fluid. Note that if the large-scale forcing were the only field acting on the spout, than the growth of the spout would simply have been reversed when the sense of the straining motion was reversed. Thus the presence of the eddy field must play an important role in this irreversible process. The distortions of the spout by the eddy field are enhanced during the horizontally dilational phase of the evolution.

Internal-wave packets

The observations of *Alford and Pinkel* (2000) show vertically propagating structures at depths from 150 to 350 m which they suggest may be internal wave packets. These structures have vertical extent of about 50 m with internal vertical wavelengths of about 12 m and are associated with overturning events with vertical scales of about 2 m. Recent theoretical analysis by *Thorpe* (1999) provides a criterion for determining whether the small-scale turbulence generated by the overturns in a packet will be left behind in just small patches or in continuous 'scars' much longer than the size of the packet. Stimulated by these developments, we have embarked on a numerical investigation of internal wave packets.

Assuming a constant background Brunt-Väisälä frequency N and ignoring the effects of the earth's rotation, the intrinsic dimensional frequency for internal waves is

$$\sigma = N \frac{k_h}{k}. \quad (21)$$

The observed frequency for one of the wavepackets in the *Alford and Pinkel* (2000) data is 4 cph. This is higher than the ambient $N \approx 3$ cph. Since $\sigma_{max} = N$, it is assumed that the observed frequency for this packet is the sum of the intrinsic frequency plus a Doppler shift. To predict this shift, it is necessary to know the wavelength of the packet, the magnitude of the ambient current and its direction relative to the packet propagation direction. *Alford and Pinkel* (2000) suggest that the intrinsic frequency for their packet with observed frequency of 4 cph is near 0.14 cph which leads one to a wavelength of 180 m. This suggests that the horizontal wavelengths in both directions are much larger than the vertical wavelength. For our numerical modeling, this

represents a difficulty. We are reluctant to introduce anisotropic grids for fear of the distortions that might result, especially when applying simple sub-grid scale models. Thus, in this preliminary work, we decided to consider only the case in which horizontal and vertical wavelengths were equal. The corresponding intrinsic frequency would then be about 2 cph which would still be consistent with the observed packet, just requiring less of a Doppler shift to match the observed frequency.

As for the amplitude of the observed packets, this can be given in terms of the peak magnitude of the observed strain rate $\partial w / \partial z$. The maximum value of vertical strain rate in the *Alford and Pinkel* (2000) observations is approximately N , and in the case of the particular packet discussed above, it seems that the maximum is about $0.38N$.

In what follows, we will examine the evolution of a particular wave packet with two-dimensional simulations. In an attempt to reproduce the kind of behavior evident in the observations, we used simulations in a domain of 200 m in both width and depth. We used a packet with non-dimensional wavenumbers of 12 in both directions, corresponding to vertical and horizontal wavelengths of $(200 \text{ m})/12 \approx 17 \text{ m}$. Our 2D simulations had an effective resolution corresponding to a cut-off wavelength of $\approx 0.8 \text{ m}$. To follow this phenomenon in DNS with all relevant scales well resolved would require resolution from 200 m down to a few cm, which is somewhat impractical. Since the subgrid scale model used in the 3D simulations is not appropriate in 2D, we had recourse to hyperviscosity (with the Laplacian taken to the eighth power). The simulations illustrated here are from a spectral code dealiased with the 3/2 rule (*Orszag* 1971). Although there are 768 wavevectors used in each direction, after application of the 3/2 rule this leaves only 512 active modes in each direction.

Linear dispersion of packets

The linearized version of the Boussinesq evolution equations can be used to obtain a model of the internal wave packet. The vorticity and density of a plane internal wave can be written dimensionally as

$$(\omega_x, \omega_y, \omega_z, \rho') = A e_{\mathbf{k}} \exp i(\mathbf{k} \cdot \mathbf{r} - \sigma t), \quad (22)$$

where A is an arbitrary amplitude and e is the eigenvector

$$e_{\mathbf{k}} = (g k_y / N k_h, -g k_x / N k_h, 0, \rho_0). \quad (23)$$

Taking a linear superposition of such waves distributed continuously in wavevector space and centered on a particular wavevector, say \mathbf{k}_0 , would produce an internal

wave packet. For example,

$$(\omega, \rho') = \mathcal{R} e \int G(\mathbf{k} - \mathbf{k}_0) e_{\mathbf{k}} e^{i(\mathbf{k} \cdot \mathbf{r} - \sigma t)} d^3 k, \quad (24)$$

with

$$G(\mathbf{p}) \equiv A \exp(-a^2 p_x^2 - b^2 p_y^2 - c^2 p_z^2), \quad (25)$$

where a , b , and c are length scales, represents a propagating ellipsoidal packet. A slight generalization based on simple coordinate rotations will also permit an arbitrary choice for the orientation of the ellipsoidal envelope relative to the crests internal to the packet. Within the envelope, the vorticity and density fields will have a phase velocity in the direction of \mathbf{k}_0 and group velocity

$$\mathbf{c}_g = \nabla_{\mathbf{k}} \sigma_{\mathbf{k}}, \quad (26)$$

which is perpendicular to the phase velocity.

By varying the dimensions a , b and c , we can change the shape of the packet as needed. A likely candidate for the packets whose effects are observed in *Alford and Pinkel's* (2000) data would suggest that at least one of these lengthscales is very large. For the present calculations we take a to be infinite. Then we chose b and c and the orientation of the system to be such that the envelope is an ellipse with major axis aligned along the direction of propagation. Other choices may also be of interest, but that will be explored in future work. With the ellipse as chosen, the phase velocity is directed along the short axis and the group velocity along the long axis. In a numerical simulation, the packet can only be approximated, with the integral replaced by a discrete sum of wavevectors. By using (24) and (25) with $t = 0$, we are able to construct the initial condition for a packet that is both reasonably confined in space and well resolved internally.

The first issue that we need to address is the dispersive spreading of the wave packet. Simple arguments suggest that the physical extent of the wave packet will grow as $\Delta c_g t$ in the direction of the group velocity, where Δc_g represents the spread in group velocities calculated for the individual wavevectors that contribute significantly to the wave packet. We can make some crude dimensional estimates for the rate of dispersion by setting $c_g \sim N/k_0$ and $\Delta c_g \sim (N/k_0^2) \Delta k_0$, where Δk_0 measures the spread of wavenumbers in the packet. If we call Δx_0 , the initial length of the wavepacket, then the change in the size of the packet can be crudely taken as

$$\Delta x - \Delta x_0 = \Delta c_g t. \quad (27)$$

The packet would then double in size by a time $t_d \sim \Delta x_0 / \Delta c_g$, and the distance that the packet can travel before doubling is

$$x / \Delta x_0 \sim k_0 / \Delta k_0. \quad (28)$$

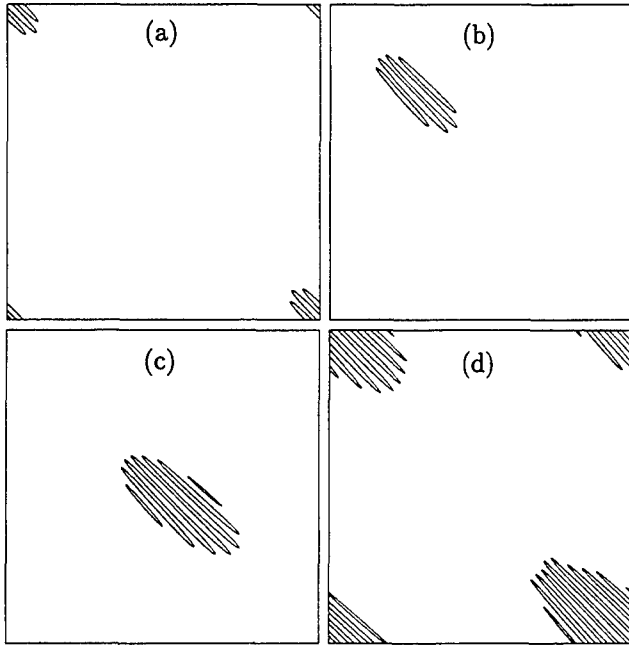


Figure 8. Contours of the magnitude of the perturbation density $|\rho'/\rho_0|$ from a simulation of the linear propagation of a wavepacket. The domain size is 200 m on each side. The vertical axis is depth. The only contour level drawn is that at 0.5 of the maximum field value. The time sequence of the panels is (a) $t=0$, (b) $t=3$ hr, (c) $t=6$ hr, and (d) 11 hr.

For the packet used in the simulations this predicts a doubling after propagation of about 200 m.

In Figure 8, we show the evolution of the density perturbation field during the propagation of our packet following purely linear dynamics. In each panel, only the contour level corresponding to $0.5|\rho'/\rho_0|$ is drawn. Positive and negative values have not been indicated, but clearly the sign of ρ' will alternate from one wave crest to the next. We see the packet propagates along the diagonal. This is in agreement with the fact that the wavevector is $\mathbf{k} = (12, 12)$ and that the group velocity is perpendicular to this. It is less obvious from the few panels that we can include here that the phase of the waves within the packet advances in the direction of \mathbf{k} . The average speed of the packet in propagating from one corner of the domain to the opposite corner is correctly given by $|c_g|$. Furthermore, we see that the width and length of the packet grow to a little more than double their original values in the time it takes to cross from one corner of the domain to the other, and this is correctly predicted by the formula (28). During the period of evolution illustrated, the peak amplitude of the packet decays to 25% of its initial value.

Although the amplitude of the packet can be changed

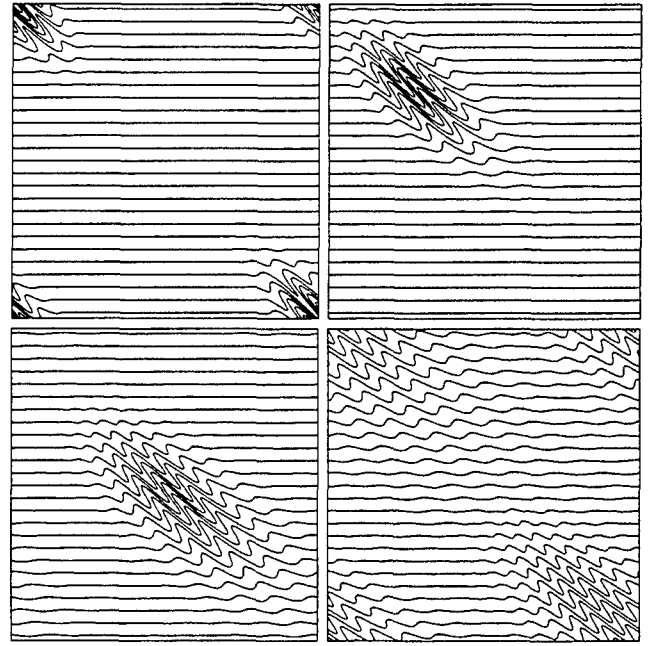


Figure 9. Contours of ρ/ρ_0 from a simulation of the linear propagation of a wavepacket. The domain size is 200 m on each side. The vertical axis is depth. The time sequence of the panels is the same as in Figure 8. The contour increment is such that the vertical separation between unperturbed isopycnals is 8 m.

arbitrarily in this purely linear simulation, we may simply assign an amplitude to see the effect of such a packet on the full density field. This is done in Figure 9. The amplitude used represents fluctuations in $\partial w/\partial z$ about five times the maximum actually observed in the *Alford and Pinkel* (2000) data. Nevertheless, we have used this packet with exaggerated amplitude to more clearly illustrate the nature of the linear propagation. In such a strong packet, there are regions of strong overturning, which, if the packet is not propagating too rapidly, would develop convective instability under the full nonlinear dynamics.

Nonlinear propagation of packets

Having determined that our packet propagates correctly under linear dynamics, we then investigated its evolution with the complete Boussinesq equations. The amplitude of the observed packet discussed in the introduction is such that the maximum value of the strain rate $\partial w/\partial z$ is about $0.38N$. With the packet amplitude set to match this value as its maximum $\partial w/\partial z$, we performed the simulation illustrated by contour plots of ρ'/ρ in Figure 10. This figure should be compared to

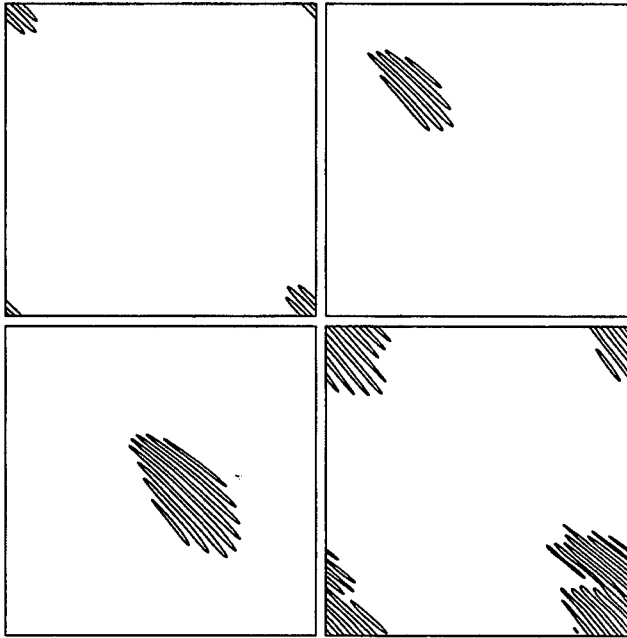


Figure 10. Contours of the magnitude of the perturbation density $|\rho'/\rho_0|$ from a simulation of the nonlinear propagation of a wavepacket with $\max \partial w/\partial z \approx 0.38N$. The domain size is 200 m on each side. The vertical axis is depth. The only contour level drawn is that at 0.5 of the maximum field value. The time sequence of the panels is the same as in Figure 8.

the corresponding figure for linear evolution, Figure 8. The times represented are the same in each figure. By the time of panel (b) a clear asymmetry in the form of the packet has developed in the nonlinear case and there is some clear distortion of the packet in the final panel. Nevertheless, the overall evolution of this nonlinear packet is not very different from the linear case. This packet is so weak that the initial condition is not overturning anywhere and the Richardson number is above 1 everywhere. Thus, the classical criteria for convective instability and shear instability are not satisfied in this packet. This continues to be the case throughout the simulation in spite of small-scale generation by nonlinear wave-wave interactions. An idea of how weak this packet is can be obtained graphically from the plots of the density contours as illustrated in Figure 11.

The next case that we will treat is one for which the amplitude of the packet is just above the threshold for overturning. The amplitude of this packet in terms of its maximum strain rate is $\partial w/\partial z = 0.76N$. In Figure 12,

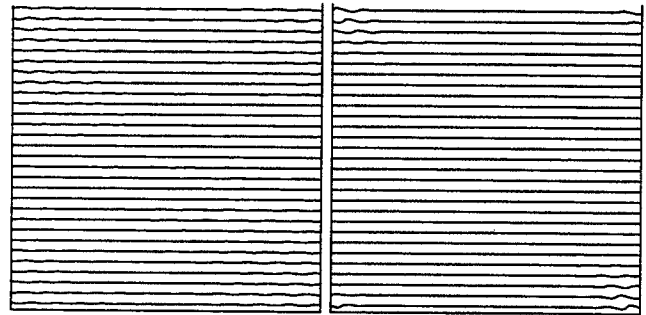


Figure 11. Contours of ρ/ρ_0 from the same simulation as represented in Figure 10. The domain size is 200 m on each side. The vertical axis is depth. The two times illustrated correspond to the first and last times of Figure 10. The contour increment is such that the vertical separation between unperturbed isopycnals is 8 m.

we display the contour plots for the perturbation density at the same times as in the previous figures. We see that there is some early production of small scales that are evident in the wake of the packet. By $t = 6$ hr the packet itself has become badly distorted, and by $t = 11$ hr, it has degenerated into small-scale structures, although these still retain to some extent an organization and alignment related to the original structure of the packet. To better illustrate the decay of this packet, we display contour plots of the full density field from $t = 2.5$ hr to $t = 4.8$ hr in Figure 13. Each frame is an enlarged image centered on the wave packet, showing only a portion of the domain (a square of size 200/3 m on a side). In panel (a) we see an early stage in which the wave is overturning at points, but there has not yet been any strong production of energy in scales smaller than 2 m (note that the spacing between the unperturbed isopycnals is 2 m). There are four relatively strong crests evident in panel (a). These crests

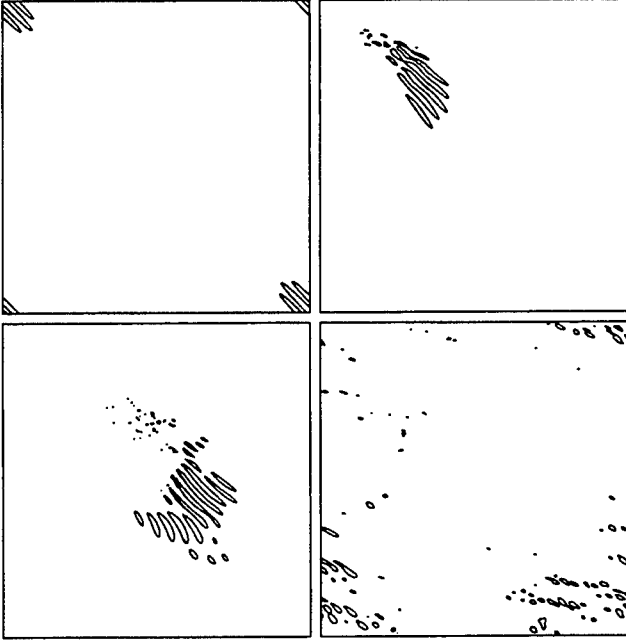


Figure 12. Contours of the magnitude of the perturbation density $|\rho'/\rho_0|$ from a simulation of the nonlinear propagation of a wavepacket with $\max \partial w/\partial z \approx 0.76N$. The domain size is 200 m on each side. The vertical axis is depth. The only contour level drawn is that at 0.5 of the maximum field value. The time sequence of the panels is the same as in Figure 8.

are advancing from bottom-left to top-right in these figures. The weakest crest (bottom-left) is just entering the packet in panel (a). In the linear evolution as each crest passes through the packet from bottom-left to top-right, its amplitude first increases and then decreases. As envisioned by Thorpe (1999), the crests amplify as they move toward the center of the packet and break leaving small-scale perturbations behind that link up with the ‘debris’ produced by the passage of previous crests. The period of the sequence of panels shown here is long enough for the weak crest on the lower-left side of the packet in panel (a) to move completely through the packet, finally becoming the weak crest on the upper-right side. In the case we have simulated here, the crests do produce overlapping zones of small-scale perturbations that form a somewhat continuous scar, a possibility suggested by Thorpe (1999). One should note, however, that during the period when a particular crest is actually breaking, the overturning and small-scale production is not uniform along the length of the crest, as assumed in Thorpe’s idealized model, but rather appears in spots along the crest (see panels (c) and (d)). Also the breaking and subsequent scar formation does

not continue indefinitely. The strength of the packet is both dispersed and dissipated, so that by $t = 210N^{-1}$ the process of scar formation has ceased.

We have also performed 3D simulations of the propagation of these wave packets. The general evolution exhibited in the 2D simulations is also found in 3D, although in 3D we did not have sufficient resolution adequately capture the 2 m overturns. Further details can be found in Carnevale and Orlandi (2000).

Theory of packet evolution

We have addressed here questions about the longevity of wave groups. A theory for the evolution of the packet envelope has been developed by Shrira (1981) via multiscale analysis in both space and time. His result for the evolution of the amplitude A of the packet in the two-dimensional case studied above is

$$iA_\tau + \{\sigma_{k_y k_y} A_{yy} + 2\sigma_{k_y k_z} A_{yz} + \sigma_{k_z k_z} A_{zz}\} - \frac{i}{6} \{\sigma_{k_y k_y k_y} A_{yyy} + 3\sigma_{k_y k_y k_z} A_{yyz} + 3\sigma_{k_y k_z k_z} A_{yzz} + \sigma_{k_z k_z k_z} A_{zzz}\} = -i\gamma A(AA_s^* - A^*A_s), \quad (29)$$

where k_y and k_z are components of the central wavevector of the packet, σ is the intrinsic frequency corresponding to the central wavevector, s is the coordinate in the direction of propagation of the packet, $\partial/\partial\tau = \partial/\partial t + c_g \partial/\partial s$, c_g is the magnitude of the group velocity, and

$$\gamma = k^3/(\sigma k_y k_z). \quad (30)$$

The typical equation that arises for the evolution of a wave-packet envelope is the cubic Schroedinger equation which is significantly different from (29). It turns out that the term corresponding to the nonlinearity in the cubic Schroedinger vanishes identically here due to the fact that a plane wave cannot interact with itself. Thus Shrira had to go to third order in the multiple scale analysis to obtain the first contributions of the nonlinearity to the evolution. This still involves a cubic term for the nonlinearity, but now not the simple $A|A|^2$ of the cubic Schroedinger equation, and the presence of the third order spatial derivatives from the linear terms further complicates matters. Notice that the coefficients depend in magnitude and sign on the orientation of the central wavevector of the packet. Thus we can anticipate interesting results as this wavevector is varied. In addition, there are nonlocal nonlinear terms that arise if the flow is three dimensional that further greatly complicate the evolution. In future work, we plan to investigate the evolution of the packet analytically based on Shrira’s equations, and make a comparison with our numerical results.

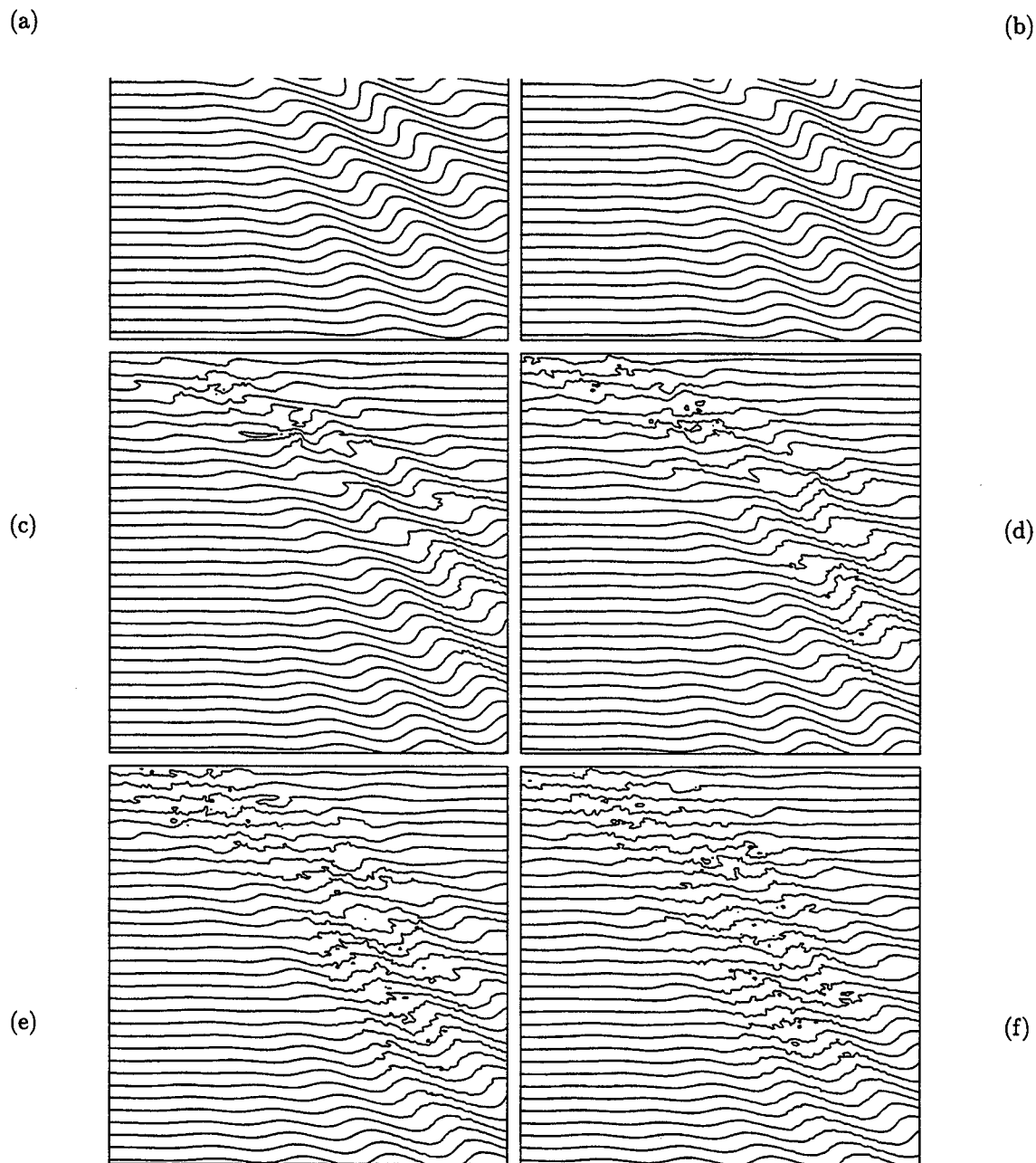


Figure 13. Contours of ρ/ρ_0 from a simulation of the nonlinear propagation of a wavepacket with initially $\max \partial w / \partial z \approx 0.76N$. Only a portion of the computational frame is shown, and this corresponds to a square 200/3 m on each side. The contour increment is such that the vertical separation between unperturbed isopycnals is 2 m. The times corresponding to the panels are (a) 2.5, (b) 2.9 (c) 3.5, (d) 3.9, (e) 4.4 and (f) 4.8 hr.

Conclusions

We have attempted with some very idealized numerical modelling to shed some light on the structures that may be responsible for the variability observed in the oceanic thermocline. This attempt has been successful to a certain extent. We were able to show a transition from buoyancy to inertial range that follows the features of the observed spectra, but only during a breaking event. To what extent this simulated transition is related to the actual transition in the oceanic observations is still not clear. We were able to give three-dimensional structure to a classical shear type instability much as found in the observations and at about the correct vertical scale. In addition, we described an unexpected kind of overturning and mixing that occurs in regions of high strain rate. The correlation for overturns and high strain rate was suggested by *Alford and Pinkel* (2000), and yet it is not clear at this point whether the structures we were able to simulate are directly related to any of the overturns reported in that paper. Finally, two-dimensional simulations demonstrated that a packet with approximately the correct vertical structure can propagate through a substantial portion of a thermocline as observed by *Alford and Pinkel* (2000) without dispersing radically and with the production of overturns on the scale of about 2 m which is entirely consistent with *Alford and Pinkel's* observations. Unfortunately, these simulations could not also capture the large horizontal scales nor the rapid advection of packets that is suggested by *Alford and Pinkel* (2000). Thus, we feel that there has been some progress in demonstrating the possibility of analyzing the small-scale fluctuations in the thermocline with numerical simulations using subgrid scale parameterizations, and look forward to advancing this work so that closer comparisons with observations may be possible.

Acknowledgments

This research has been supported by Office of Naval Research grants N00014-97-1-0095 and N00014-96-0762. Numerical simulations were performed at the San Diego Super Computer Center and the Center for Turbulence Research, Stanford. We thank the staff of the San Diego Supercomputer Center for help in preparing the three-dimensional images for this paper and the animation used in this research. Additional computing support was provided by the Office of Naval Research and the University of Rome. We thank Matthew Alford, Lou Goodman, Myrl Hendershott, Greg Holloway, James Lerczac, Robert Pinkel and David Siegel for very helpful discussions and suggestions.

References

- Alford, M., and R. Pinkel, Observations of overturning in the thermocline: the context of ocean mixing. *J. Phys. Oceanogr.*, **30**, 805-832, 2000.
- Bouruet-Aubertot, P., J. Sommeria, and C. Staquet, Breaking of standing internal gravity waves through two-dimensional instabilities. *J. Fluid Mech.*, **285**, 265-301, 1995.
- Bouruet-Aubertot, P., J. Sommeria, and C. Staquet, Stratified turbulence produced by internal wave breaking: two-dimensional numerical experiments. (4th International Symposium on Stratified Flows, Grenoble, France, 29 June-2 July 1994). *Dyn. Atmos. Oceans*, **23**, 357-69, 1996.
- Carnevale, G.F., and M. Briscolini, Large Eddy Simulation of Oceanic Fine Structure, 'Aha Huliko'a, Internal Wave Modeling, Proceedings, Hawaiian Winter Workshop, University of Hawaii, January 19-22, 1999 eds. P. Muller and D. Henderson, pp. 279-288, 1999.
- Carnevale, G.F. and P. Orlandi, Propagation of internal wave packets in the thermocline, Proceedings of the 2000 Summer Program, Center for Turbulence Research, Stanford University pp. 119-130, 2000.
- Carnevale, G.F., M. Briscolini, M., and P. Orlandi, Buoyancy to inertial range transition in forced stratified turbulence *J. Fluid Mech.*, **427**, 05-239, 2001.
- Gargett, A.E., P.J. Hndricks, T.B. Sanford, T.R. Osborn, and A.J. Williams, A composite spectrum of vertical shear in the upper ocean. *J. Phys. Oceanogr.*, **11**, 1258-1271, 1981.
- Gargett, A.E., Evolution of scalar spectra with the decay of turbulence in a stratified fluid. *J. Fluid Mech.*, **159**, 397-407, 1985.
- Garrett, C., and W. Munk, Space-time scales of internal waves: A progress report. *J. Geophys. Res.*, **80**, 291-297, 1975.
- Gibson, C.H., Internal waves, fossil turbulence, and composite ocean microstructure spectra. *J. Fluid Mech.*, **168**, 89-117, 1986.
- Gregg, M.C., Variations in the intensity of small-scale mixing in the main thermocline (Pacific Ocean). *J. Phys. Oceanogr.*, **7**, 436-454, 1977.
- Gregg, M.C., Scaling turbulent dissipation in the thermocline. *J. Geophys. Res.*, **94**, 9686-9698, 1989.
- Herring, J.R., and O. Metais, Spectral transfer and bispectra for turbulence with passive scalars. *J. Fluid Mech.*, **235**, 103-121, 1992.
- Holloway, G., Theoretical approaches to interactions among internal waves, turbulence and finestructure. in *Nonlinear Properties of Internal Waves*, AIP conference proceedings No. 76, (ed. B.J. West, AIP, New

- York), 1981.
- Holloway, G., A conjecture relating oceanic internal waves and small-scale processes. *Atmos. Ocean.*, **21**, 107-122, 1983.
- Holloway, G., Considerations on the theory of temperature spectra in stably stratified turbulence. *J. Physical. Oceanogr.*, **16**, 2179-2183, 1986.
- Holloway, G., The buoyancy flux from internal gravity wave breaking. *Dyn. Atmos. Oceans*, **12**, 107-125, 1988.
- Kaltenbach, H.-J., T. Gerz, and U. Schumann, Large-eddy simulation of homogeneous turbulence and diffusion in stably stratified shear flow. *J. Fluid Mech.*, **280**, 1-40, 1994.
- Lesieur, M., and R. Rogallo, Large-eddy simulation of passive scalar diffusion in isotropic turbulence. *Phys. Fluids A*, **1**, 718-722, 1989.
- Lesieur, M., *Turbulence in Fluids*, Dordrecht; Boston, Kluwer Academic Publishers, 1997.
- Lumley, J.L., The spectrum of nearly inertial turbulence in a stable stratified fluid, *J. Atmos. Sci.*, **21**, 99-102, 1964.
- Lumley, J.L., 1967 Theoretical aspects of research on turbulence in stratified flows, in *Atmospheric Turbulence and Radio Wave Propagation*, Proceedings of the International Colloquium, Moscow 1965 (A.M. Yaglom and V.I. Tatarsky, Eds), *Nauka*, Moscow, 121-128, 1967.
- McEwan, A.D., The kinematics of stratified mixing through internal wavebreaking, *J. Fluid Mech.*, **128**, 47-57, 1983.
- Orszag, S.A., On the elimination of aliasing in finite-difference schemes by filtering high-wavenumber components, *J. Atmos. Sci.*, **28**, 1074, 1971.
- Phillips, O.M., On the Bolgiano and Lumley-Shur theories of the buoyancy subrange. *Atmospheric Turbulence and Radio Wave Propagation* Proceedings of the International Colloquium, Moscow 1965 (A.M. Yaglom and V.I. Tatarsky, Eds), *Nauka*, Moscow, 121-128, 1967.
- Ramsden, D., and G. Holloway, Energy transfers across an internal wave-vortical mode spectrum. *J. Geophys. Res.*, **97**, 3659-3668, 1992.
- Siegel, D.A., and J.A. Domaradzki, Large-eddy simulation of decaying stably stratified turbulence, *J. Phys. Oceanogr.*, **24**, 2353-86, 1994.
- Shrira, V.I., On the propagation of a three-dimensional packet of weakly non-linear internal gravity waves. *Int. J. Non-Linear Mech.*, **16**, 129-138, 1981.
- Taylor, J.R., The energetics of breaking events in a resonantly forced internal wave field, *J. Fluid Mech.*, **239**, 309-340, 1992.
- Thorpe, S.A., On internal wave groups, *J. Phys. Oceanogr.*, **29**, 1085-1095, 1999.
- Weinstock, J., On the theory of temperature spectra in a stably stratified fluid. *J. Phys. Oceanogr.*, **15**, 475-477, 1985.